

Kernel Space Diffusion Model for Efficient Remote Sensing Pansharpening

Hancong Jin¹ Zihan Cao¹ Liangjian Deng^{1*}

¹University of Electronic Science and Technology of China

Abstract

Pansharpening is a fundamental task in remote sensing that integrates high-resolution panchromatic imagery (PAN) with low-resolution multispectral imagery (LRMS) to produce an enhanced image with both high spatial and spectral resolution. Despite significant progress in deep learning-based approaches, existing methods often fail to capture the global priors inherent in remote sensing data distributions. Diffusion-based models have recently emerged as promising solutions due to their powerful distribution mapping capabilities; however, they suffer from significant inference latency, which limits their practical applicability. In this work, we propose the Kernel Space Diffusion Model (KSDiff), a novel approach that leverages diffusion processes in a latent space to generate convolutional kernels enriched with global contextual information, thereby improving pansharpening quality while enabling faster inference. Specifically, KSDiff constructs these kernels through the integration of a low-rank core tensor generator and a unified factor generator, orchestrated by a structure-aware multi-head attention mechanism. We further introduce a two-stage training strategy tailored for pansharpening, enabling KSDiff to serve as a framework for enhancing existing pansharpening architectures. Experiments on three widely used datasets, including WorldView-3, GaoFen-2, and QuickBird, demonstrate the superior performance of KSDiff both qualitatively and quantitatively. Code will be released upon possible acceptance.

1 Introduction

Due to the inherent physical limitations of satellite sensors, the direct acquisition of high-resolution multispectral images (HRMS) is not feasible. Instead, sensors typically provide high-resolution panchromatic (PAN) images and low-resolution multispectral images (LRMS). Pansharpening techniques aim to fuse the spatial detail of PAN images with the spectral richness of LRMS, thereby generating HRMS with enhanced spatial and spectral fidelity. As a foundational preprocessing approach, pansharpening plays a critical role in numerous remote sensing applications, including image segmentation [61] and change detection [55].

Over the past decades, a variety of pansharpening techniques have been proposed, which can be broadly categorized into four families: component substitution (CS) [22, 32], multi-resolution analysis (MRA) [33, 48], variational optimization (VO) [57, 58], and deep learning (DL)-based methods. While classical CS and MRA methods offer interpretable mathematical formulations, they often introduce noticeable spectral or spatial distortions due to oversimplified assumptions. VO-based methods improve flexibility by formulating pansharpening as an optimization problem with prior constraints, but their performance is sensitive to model design and hyperparameters.

In recent years, deep learning, particularly convolutional neural networks (CNNs), has emerged as a powerful paradigm for pansharpening, achieving impressive performance across benchmark

*Corresponding author

datasets. Representative approaches such as PanNet [60], DiCNN [14], and FusionNet [8] model the fusion process as a non-linear mapping from PAN and LRMS inputs to an HRMS output. These methods typically rely on improved architectural designs [56, 23] or more effective modules [17, 10] to enhance learning capacity. Most existing deep learning-based models are deterministic, which enables fast inference but limits their capacity to capture global statistical dependencies and the complex high-dimensional data distributions inherent in remote sensing imagery.

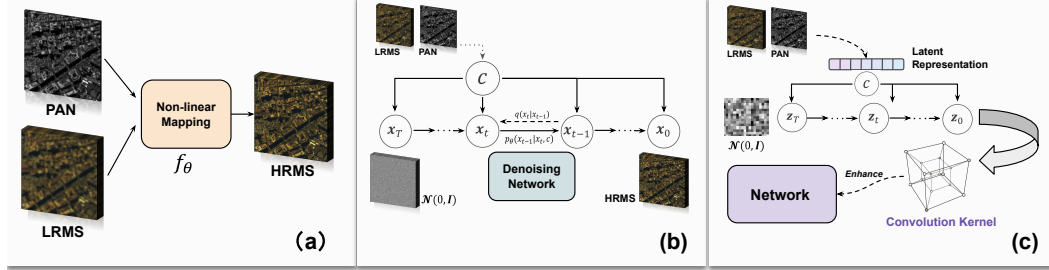


Figure 1: (a) Traditional DL-based methods directly learn a non-linear mapping f_θ to fuse PAN and LRMS images in a one-step manner. (b) The denoising diffusion model employs a multi-step refinement process conditioned on PAN and LRMS from pure Gaussian noise $\mathcal{N}(0, \mathbf{I})$. The $q(\mathbf{x}_t|\mathbf{x}_{t-1})$, $p_\theta(\mathbf{x}_{t-1}|\mathbf{x}_t, \mathbf{c})$ and \mathbf{c} denote the noise adding process, the reverse denoising process, and the condition, respectively. (c) The proposed KSDiff, which generates convolution kernels to enhance regression-based pansharpening networks via a diffusion model performing in the latent space.

Diffusion models [15, 18, 38], rooted in generative modeling, learn complex data distributions through iterative denoising steps, reconstructing samples from Gaussian noise. Unlike conventional deep learning methods mentioned above, they model the full conditional distribution of outputs given inputs, enabling flexible, context-aware generation. This makes them ideal for pansharpening, as they integrate heterogeneous inputs like PAN and LRMS images to produce spectrally consistent, high-resolution multispectral images with high fidelity [31, 5]. However, a common limitation of diffusion-based methods lies in their slow inference speed due to the iterative nature of the sampling process [41, 18]. This latency issue becomes particularly critical in the pansharpening task, where the target images are of high resolution and the input data typically contains more channels than standard RGB images. These factors significantly increase the difficulty of distribution mapping within diffusion models. Moreover, in the context of pansharpening, where most spatial and spectral information is already available, the role of the network is primarily to refine rather than reconstruct from scratch. Consequently, reconstructing the entire image from pure Gaussian noise is both counterintuitive and burdensome.

Considering the respective strengths and limitations of traditional deep learning methods and diffusion-based approaches for pansharpening, we propose a novel framework named KSDiff. KSDiff leverages the powerful distribution modeling capability of diffusion processes to enrich convolutional kernels with high-level remote sensing context, while preserving the inference efficiency of conventional DL-based methods. Specifically, we train a diffusion process in latent space [35, 59], significantly reducing the computational burden compared to modeling the diffusion process in the full pixel space and ensuring efficient inference. The generated latent representations are then used to construct low-rank convolutional cores, which are subsequently expanded into full convolutional kernels via a structure-aware multi-head attention mechanism that integrates the generated convolution cores with features extracted from the PAN and LRMS images, as shown in Fig. 3. To effectively train KSDiff with regression backbones, we further introduce a two-stage training scheme and a Pyramid Latent Fusion Encoder (PLFE) tailored to the pansharpening task. KSDiff can be integrated into existing networks, boosting performance over baselines. Remarkably, it achieves inference speeds comparable to traditional DL methods, orders of magnitude faster than recent diffusion-based pansharpening approaches. Our main contributions are as follows:

- We propose KSDiff, a novel framework that integrates diffusion-generated latent representation into the design of convolutional kernels. This approach leverages the strong distribution modeling capabilities of diffusion models while achieving fast inference speed.

- We introduce a two-stage training scheme and a Pyramid Latent Fusion Encoder (PLFE) specifically tailored for pansharpening. These components enable effective integration of multi-scale spatial-spectral information and allow KSDiff to be incorporated into existing regression-based networks.
- We conduct extensive experiments on multiple benchmark datasets, demonstrating that KSDiff achieves competitive performance in both quantitative metrics and visual quality. In addition, it offers inference speeds comparable to traditional DL-based methods and significantly faster than recent diffusion-based pansharpening approaches.

2 Related Works

2.1 Deep Learning Based Methods

PNN [30] was the first to apply CNNs to pansharpening, inspired by single-image super-resolution techniques. To better preserve high-frequency details, PanNet [60] introduced a strategy that injects high-pass PAN information into the upsampled LRMS image. DiCNN [14] further enhanced detail preservation using a detail-injection framework, while FusionNet [8] employed a residual network to explicitly learn high-frequency components. Subsequent works, such as DCFNet [56] and PMACNet [23], improved CNN architectures and achieved superior performance. CTINN [66] adopted a transformer-based design to capture long-range dependencies in the fusion process. To address the limitations of static convolutional kernels, LAGConv [17] introduced dynamic kernels conditioned on the input. Building on this idea, AKD [34] proposed dual dynamically generated branches for extracting spatial and spectral details. Another branch of methods delved into frequency domain analysis of PAN and LRMS images, such as HFIN [44]. These advancements have significantly expanded the research scope of DL-based pansharpening methods.

2.2 Diffusion Models

Diffusion models (DMs) [15, 42] have recently advanced generative modeling by formulating data synthesis as a sequence of denoising steps. While initially applied to image generation [15], subsequent developments enabled high-resolution synthesis [35], multimodal conditioning [11], and efficient sampling [41, 63]. DMs have also shown strong promise in low-level vision tasks. StableSR [52] achieved real-world image super-resolution by leveraging the prior knowledge from large pre-trained text-to-image latent diffusion model. DiffIR [59] combined the training of a transformer with a diffusion model for realistic image restoration. DPS [6] introduced zero-shot posterior sampling for general inverse problems. In pansharpening, most methods [31, 5, 37] use conditional diffusion models [38] in pixel space, conditioning on PAN and LRMS to iteratively generate HRMS outputs. Recent theory [2] unifies diffusion, flow matching [24], and diffusion-bridge models [65, 7] under stochastic differential equations (SDEs) and ordinary differential equations (ODEs), enabling flexible distribution mapping. However, solving these SDEs/ODEs demands many network function evaluations (NFEs), incurring high computational cost. Acceleration strategies, such as advanced samplers [18, 39] and distillation techniques [26, 43], reduce NFEs but either require full model retraining or lead to performance trade-offs. Some recent work further explores the versatile use of diffusion models. For example, Neural Network Diffusion [53] employs an autoencoder–diffusion pipeline to synthesize latent representations of network parameters and decode them into novel, high-performing weights.

3 Methodology

In this section, we present the design of the kernel generator in our proposed KSDiff, as well as a two-stage training scheme tailored for the pansharpening task. Fig. 3 illustrates the architecture of the KSDiff kernel generator. Fig. 2 depicts the two-stage training pipeline and the latent fusion encoder. We introduce our method following the order of training procedures.

3.1 Pre-training Stage

In the pre-training stage, our objective is to encode the ground truth high-resolution multispectral (HRMS) image into a compact latent representation, which is then utilized to guide the convolutional

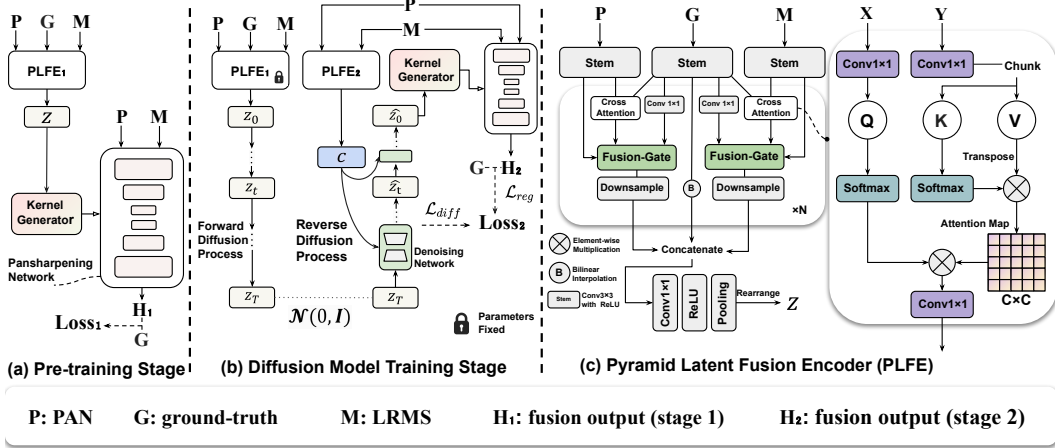


Figure 2: An overview of our two-stage training procedure and the structure of the Pyramid Latent Fusion Encoder (PLFE). (a) **Pre-training Stage**: The goal is to extract a latent representation \mathbf{z} by optimizing PLFE_1 jointly with the kernel generator and the pansharpener network. (b) **Diffusion Model Training Stage**: The latent representation \mathbf{z}_0 , extracted by the pre-trained PLFE_1 , is predicted by leveraging the strong distribution estimation ability of the diffusion model (no ground truth is used as input for its denoising network). (c) **PLFE**: The figure only shows the structure of PLFE_1 ; since PLFE_2 only takes \mathbf{P} and \mathbf{M} as input, its structure is slightly different (a halved version compared to PLFE_1). Further details can be found in the Suppl. Sec. B. At inference time, only PLFE_2 , the reverse diffusion process, the kernel generator, and the pansharpener network are involved.

kernels within pansharpener networks during image fusion. As illustrated in Figs. 3 and Figs. 2, we employ a Pyramid Latent Fusion Encoder (PLFE) to compress the ground truth HRMS image and extract a compact prior feature. This prior feature is subsequently used to generate low-rank convolutional core tensors (*i.e.*, \mathcal{G} in Fig. 3), from which full convolutional kernels are reconstructed. By incorporating this learned prior, our method enables kernel-wise guidance across the pansharpener network, thereby enhancing the fidelity and spatial-spectral consistency of the reconstructed multispectral image. The components of this framework are described in detail below.

Pyramid Latent Fusion Encoder (PLFE). To fully leverage the complementary priors of the PAN, LRMS and HRMS modalities while avoiding the spatial-spectral entanglement inherent in naive concatenation, we introduce the Pyramid Latent Fusion Encoder (PLFE). Its design is driven by two principles: first, a multi-scale pyramid architecture in which PAN and LRMS features are progressively refined under HRMS guidance at each level, integrating high-resolution spatial cues with contextual spectral semantics; and second, a dynamic fusion gate that adaptively balances the contributions of the original branch features and the HRMS-guided features to maintain spatial-spectral consistency throughout the encoding process. Specifically, given the PAN image $\mathbf{P} \in \mathbb{R}^{H \times W \times 1}$, the LRMS image $\mathbf{M} \in \mathbb{R}^{H \times W \times C}$ and the ground-truth HRMS image $\mathbf{G} \in \mathbb{R}^{H \times W \times C}$, PLFE first embeds each via a stem block, followed by N pyramid stages to capture features at multi-scale. At a certain stage, the PAN or LRMS branch features $\mathbf{X} \in \mathbb{R}^{H' \times W' \times d}$ are refined under guidance from the HRMS feature $\mathbf{Y} \in \mathbb{R}^{H' \times W' \times d}$ using cross attention with linear complexity [40, 19], alleviating the computational burden of this dual-branch attention when facing large images. Its mechanism is as follows:

$$\begin{aligned}
 \mathbf{Q} &= \text{Reshape}(\text{Softmax}(\mathbf{Q}, 1)), \quad \mathbf{K} = \text{Reshape}(\text{Softmax}(\mathbf{K}, 2)), \quad \mathbf{V} = \text{Reshape}(\mathbf{V}), \\
 \mathbf{A} &= \mathbf{K} \odot \mathbf{V}^T, \quad \mathbf{O} = \text{Conv}_{out}(\mathbf{A}^T \odot \mathbf{Q}),
 \end{aligned} \tag{1}$$

where $\mathbf{Q}, \mathbf{K}, \mathbf{V}, \mathbf{A}, \mathbf{O}$ represent the query, key, value, attention map, and output, respectively, \odot is the elementwise multiplication. \mathbf{Q}, \mathbf{K} and \mathbf{V} are obtained from \mathbf{X} and \mathbf{Y} with several convolution layers, as depicted in Fig. 2 (c). Reshape operation flattens the spatial dimensions of \mathbf{Q}, \mathbf{K} , and \mathbf{V} , into a single dimension, *i.e.*, $\mathbb{R}^{H \times W \times d} \rightarrow \mathbb{R}^{HW \times d}$, and $\text{Softmax}(\mathbf{K}, j)$ represents the Softmax operation along the j th dimension. Consequently, the memory complexity is reduced from $\mathcal{O}((HW)^2)$ to $\mathcal{O}(d^2)$, with $d \ll HW$, compared to vanilla attention [46]. We then adaptively fuse the guidance

from the cross attention via a dynamic fusion gate:

$$\mathbf{G}_{\text{gate}} = \sigma(\text{Conv}_g[\mathbf{X}; \text{Proj}(\mathbf{Y})]), \quad \mathbf{F} = \mathbf{G}_{\text{gate}} \odot \mathbf{X} + (1 - \mathbf{G}_{\text{gate}}) \odot \text{Proj}(\mathbf{Y}) + \mathbf{O}, \quad (2)$$

where Proj is for channel alignment, σ is a Sigmoid function along channel dimension. By learning \mathbf{G}_{gate} , the network balances trusting the HRMS prior-refining features where reliable, and preserving the original branch feature where guidance may misalign, thus enhancing spatial-spectral consistency and reducing artifacts, yielding better encoding quality. A strided convolution downsamples \mathbf{F} , while \mathbf{Y} is bilinearly interpolated for the next stage. After N stages, the final features are concatenated and then projected into $\mathbf{z} \in \mathbb{R}^{S \times C_z}$, with S and C_z representing the token number and the embedded dimension respectively, obtaining a compact prior representation ($S \ll HW$) for downstream kernel modulation.

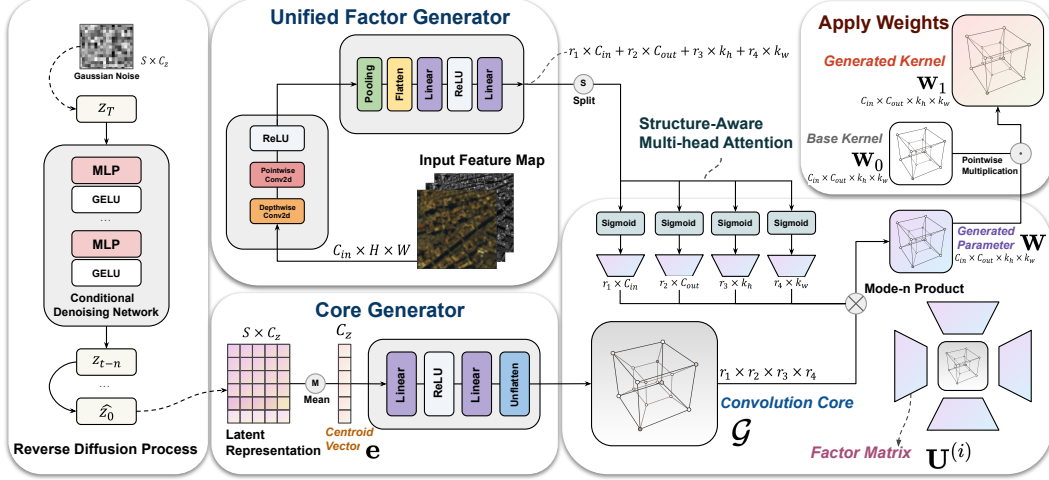


Figure 3: Kernel Generator of our proposed KSDiff. The kernel generator comprises two sub-modules: (1) a diffusion model-driven convolutional core generator, (2) a unified factor generator that takes feature maps as input. The outputs of these two modules are integrated using a structure-aware multi-head attention mechanism to reparameterize the base kernel.

Kernel Generator. We explore an efficient strategy to enrich convolutional layers with encoded latent representations that capture high-level global context. Given a convolutional kernel represented as a 4D tensor of shape $C_{\text{in}} \times C_{\text{out}} \times k_h \times k_w$ (typically with $k_h = k_w = k$), a naive solution is to flatten the latent code \mathbf{z} , pass it through a MLP, and reshape the output to obtain the convolution kernel. However, this approach introduces a prohibitive number of parameters and lacks flexibility in controlling the influence of the latent representation across different kernels within a network. To address these issues, we propose to modulate a standard base kernel $\mathbf{W}_0 \in \mathbb{R}^{C_{\text{in}} \times C_{\text{out}} \times k_h \times k_w}$ with a learned weight tensor \mathbf{W} , yielding the final kernel as $\mathbf{W}_1 = \mathbf{W}_0 \odot \mathbf{W}$, where \odot denotes element-wise multiplication. To reduce complexity, we factorize \mathbf{W} via tensor algebra [45, 21]:

$$\mathbf{W} = \mathcal{G} \times_1 \mathbf{U}^{(1)} \times_2 \mathbf{U}^{(2)} \times_3 \mathbf{U}^{(3)} \times_4 \mathbf{U}^{(4)}, \quad (3)$$

where \times_n denotes mode- n product, with a compact core tensor $\mathcal{G} \in \mathbb{R}^{r_1 \times r_2 \times r_3 \times r_4}$ and factor matrices $\{\mathbf{U}^{(n)}\}$ of size $\mathbf{U}^{(1)} \in \mathbb{R}^{r_1 \times C_{\text{in}}}$, $\mathbf{U}^{(2)} \in \mathbb{R}^{r_2 \times C_{\text{out}}}$, $\mathbf{U}^{(3)} \in \mathbb{R}^{r_3 \times k_h}$, and $\mathbf{U}^{(4)} \in \mathbb{R}^{r_4 \times k_w}$. The core tensor is generated by applying mean pooling on \mathbf{z} to obtain a centroid vector $\mathbf{e} \in \mathbb{R}^{C_z}$, which is processed by an MLP. The factor matrices are obtained from input features via a lightweight shared backbone followed by four attention heads, which we refer to as structure-aware multi-head attention, as shown in Fig. 3. This design achieves efficient, expressive kernel modulation with controllable prior influence. An experiment on the influence of different low-rank core tensor sizes is presented in Sec. 4.4. In comparison to the naive MLP-based approach with $\mathcal{O}(C_{\text{in}} C_{\text{out}} k^2 C_z)$ complexity, this formulation has $\mathcal{O}(C_z r_1 r_2 r_3 r_4 + \sum_{n=1}^4 r_n d_n)$ theoretical complexity, where d_n denotes the size of the n -th mode. With $r_n \ll d_n$, this leads to notable savings in computation and memory while supporting flexible, kernel-wise adaptation.

Pansharpening Network. By modulating low-rank core tensors of convolutional kernels, our method is suited for architectures that benefit from large kernel sizes, which have broader receptive field, extending beyond the commonly used 3×3 convolutions. We validate the effectiveness of our approach by building a U-Net [36] architecture, in which we adopt ConvNeXt blocks [27], a modern convolutional design that systematically explores large kernel configurations as the primary building blocks. We denote our network as PanNeXt-U. A detailed description of the network structure is presented in the Suppl.Sec. B.

Training Technique. To enhance the capability of the latent encoder in constructing an informative prior feature representation, we jointly optimize it alongside the kernel generator within the integrated pansharpening framework. The training objective employs an L_1 loss function, formulated as:

$$\mathcal{L}_{s1} = \|\mathbf{G} - \mathbf{H}_1\|_1, \quad (4)$$

where \mathbf{G} denotes the ground-truth high-resolution multispectral (HRMS) image, and \mathbf{H}_1 represents the reconstructed HRMS output.

3.2 Diffusion Model Training Stage

In this stage, as illustrated in Fig. 2 (b), we leverage the powerful distribution estimation capability of diffusion models to approximate the latent representation prior. Our framework adopts both DDPM [15] and DDIM [41] paradigms to formulate the forward and backward processes. While more recent advancements in diffusion scheduling [18, 24] or more efficient sampling strategies [63, 29, 62] could potentially be incorporated into our framework, we intentionally employ the classical approach to maintain both simplicity and excellent pansharpening performance.

Diffusion Model. In the forward diffusion process, given the ground-truth high-resolution multispectral (HRMS) image, we first employ the pre-trained PLFE₁ from the previous stage to obtain the corresponding prior feature $\mathbf{z}_0 \in \mathbb{R}^{S \times C_z}$, which serves as the initial state of the forward Markov chain. We then gradually add Gaussian noise over T iterations as follows:

$$q(\mathbf{z}_{1:T} | \mathbf{z}_0) = \prod_{t=1}^T q(\mathbf{z}_t | \mathbf{z}_{t-1}), \quad q(\mathbf{z}_t | \mathbf{z}_{t-1}) = \mathcal{N}(\mathbf{z}_t; \sqrt{1 - \beta_t} \mathbf{z}_{t-1}, \beta_t \mathbf{I}), \quad (5)$$

where $t = 1, \dots, T$, \mathbf{z}_t denotes the noisy feature at step t , and $\beta_{1:T} \in (0, 1)$ controls the noise schedule. By utilizing the reparameterization trick [20], one can derive the closed-form marginal:

$$q(\mathbf{z}_t | \mathbf{z}_0) = \mathcal{N}(\mathbf{z}_t; \sqrt{\bar{\alpha}_t} \mathbf{z}_0, (1 - \bar{\alpha}_t) \mathbf{I}), \quad \alpha_t = 1 - \beta_t, \quad \bar{\alpha}_t = \prod_{i=1}^t \alpha_i. \quad (6)$$

The reverse diffusion process aims to recover the prior feature from an isotropic Gaussian initialization. It is formulated as a T -step Markov chain running backward from \mathbf{z}_T to \mathbf{z}_0 . At each reverse step, the posterior distribution is given by:

$$p(\mathbf{z}_{t-1} | \mathbf{z}_t, \mathbf{z}_0) = \mathcal{N}\left(\mathbf{z}_{t-1}; \frac{1}{\sqrt{\alpha_t}} \left(\mathbf{z}_t - \frac{1 - \alpha_t}{\sqrt{1 - \bar{\alpha}_t}} \epsilon \right), \frac{1 - \bar{\alpha}_{t-1}}{1 - \bar{\alpha}_t} \beta_t \mathbf{I} \right), \quad (7)$$

where ϵ denotes the noise component in \mathbf{z}_t , which can be estimated by a denoising network ϵ_θ (see Fig. 3 and Fig. 2(b)). Since we perform diffusion in the latent space, we adopt a second PLFE, denoted PLFE₂, to condense the panchromatic image \mathbf{P} and the LRMS image \mathbf{M} into the conditional latent $\mathbf{c} \in \mathbb{R}^{S \times C_z}$. Note that PLFE₂ retains a halved structure compared to the pre-trained PLFE₁, which is symmetric (see Fig. 2(c)). To accelerate sampling, we employ the DDIM sampler [41], which operates in a non-Markovian manner:

$$\mathbf{z}_{t-n} = \sqrt{\bar{\alpha}_{t-n}} \frac{\mathbf{z}_t - \sqrt{1 - \bar{\alpha}_t} \epsilon_\theta(\mathbf{z}_t, t, \mathbf{c})}{\sqrt{\bar{\alpha}_t}} + \sqrt{1 - \bar{\alpha}_{t-n} - \sigma_t^2} \epsilon_\theta(\mathbf{z}_t, t, \mathbf{c}) + \sigma_t^2 \epsilon, \quad (8)$$

where σ_t is a predetermined function of t and n denotes the number of skipped steps. After sampling, we obtain the predicted prior $\hat{\mathbf{z}}_0 \in \mathbb{R}^{S \times C_z}$, which is then fed into the kernel generation process to guide the entire pansharpening network.

Training Technique. The training objective of standard DDPM (denoted as ϵ -prediction) often underperforms in some specific tasks [25, 5]. We therefore reparameterize the diffusion loss to predict the original sample \mathbf{z}_0 , which is mathematically equivalent to ϵ -prediction [15]. Concretely, we optimize:

$$\mathcal{L}_{\text{diff}} = \mathbb{E}_{t, \mathbf{z}_0, \mathbf{c}} [\|\mathbf{z}_0 - \mathbf{z}_\theta(\mathbf{z}_t, t, \mathbf{c})\|_1]. \quad (9)$$

We observe that jointly training the diffusion model and the pansharpening regressor yields superior high-resolution multispectral (HRMS) reconstructions compared to a separate training scheme, corroborating findings in other domains [13, 59]. Accordingly, our overall objective becomes:

$$\mathcal{L}_{s2} = \mathcal{L}_{\text{diff}} + \mathcal{L}_{\text{reg}} = \mathbb{E}_{t, \mathbf{z}_0, \mathbf{c}} [\|\mathbf{z}_0 - \mathbf{z}_\theta(\mathbf{z}_t, t, \mathbf{c})\|_1] + \|\mathbf{G} - \mathbf{H}_2\|_1, \quad (10)$$

where \mathbf{G} is the ground-truth HRMS image, and \mathbf{H}_2 denotes the pansharpened output produced during diffusion-model training. This unified loss encourages both accurate diffusion estimation and faithful spectral-spatial reconstruction in a single end-to-end framework.

3.3 Inference.

At inference time, only the reverse diffusion process is employed. The PLFE₂ module extracts a conditional code \mathbf{c} from PAN and LRMS images, which guides the sampling process starting from pure Gaussian noise $\mathbf{z}_T \in \mathbb{R}^{S \times C_z}$ through the trained conditional denoising network. The resulting latent representation is then fed into the kernel generator, enabling the pansharpening network to fuse PAN and LRMS images with the global context provided by this representation.

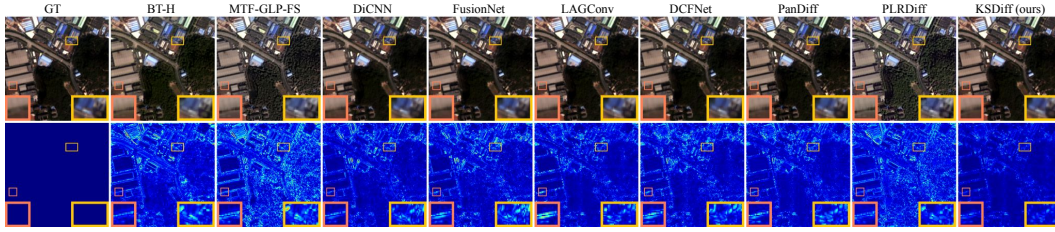


Figure 4: Comparison of qualitative results for representative methods on the GF2 reduced-resolution dataset. The first row displays RGB outputs, and the second row presents the error maps.

4 Experiments

Table 1: Result on the WV3 reduced-resolution and full-resolution datasets. The best results are highlighted in bold and the second best results are underlined.

Method	Reduced resolution				Full resolution			Runtime (s)
	SAM (\pm std)	ERGAS (\pm std)	Q2 ^a (\pm std)	SCC (\pm std)	D_λ (\pm std)	D_s (\pm std)	HQNR (\pm std)	
BDS-PC [47]	5.4675 \pm 1.7185	4.6549 \pm 1.4667	0.8117 \pm 0.1063	0.9049 \pm 0.0419	0.0625 \pm 0.0235	0.0730 \pm 0.0356	0.8698 \pm 0.0531	0.059
MTF-GLP-FS [49]	5.3233 \pm 1.6548	4.6452 \pm 1.4441	0.8177 \pm 0.1014	0.8984 \pm 0.0466	0.0206\pm0.0082	0.0630 \pm 0.0284	0.9180 \pm 0.0346	0.023
BT-H [1]	4.8985 \pm 1.3028	4.5150 \pm 1.3315	0.8182 \pm 0.1019	0.9240 \pm 0.0243	0.0574 \pm 0.0232	0.0810 \pm 0.0374	0.8670 \pm 0.0540	0.321
PNN [30]	3.6798 \pm 0.7625	2.6819 \pm 0.6475	0.8929 \pm 0.0923	0.9761 \pm 0.0075	<u>0.0213\pm0.0080</u>	0.0428 \pm 0.0147	0.9369 \pm 0.0212	0.042
DiCNN [14]	3.5929 \pm 0.7623	2.6733 \pm 0.6627	0.9004 \pm 0.0871	0.9763 \pm 0.0072	<u>0.0362\pm0.0111</u>	0.0426 \pm 0.0175	0.9195 \pm 0.0258	0.083
MSDCNN [54]	3.7773 \pm 0.8032	2.7608 \pm 0.6884	0.8900 \pm 0.0900	0.9741 \pm 0.0076	0.0230 \pm 0.0091	0.0467 \pm 0.0199	0.9316 \pm 0.0271	0.112
FusionNet [8]	3.3252 \pm 0.6978	2.4666 \pm 0.6446	0.9044 \pm 0.0904	0.9807 \pm 0.0069	0.0239 \pm 0.0090	0.0364 \pm 0.0137	0.9406 \pm 0.0197	0.065
CTINN [66]	3.2523 \pm 0.6436	2.3936 \pm 0.5194	0.9056 \pm 0.0840	0.9826 \pm 0.0064	0.0550 \pm 0.0288	0.0679 \pm 0.0312	0.8815 \pm 0.0488	1.329
LAGConv [17]	3.1042 \pm 0.5585	2.2999 \pm 0.6120	0.9098 \pm 0.0842	0.9830 \pm 0.0068	0.0368 \pm 0.0148	0.0418 \pm 0.0162	0.9230 \pm 0.0247	1.381
MMNet [67]	3.0844 \pm 0.6398	2.3428 \pm 0.6260	<u>0.9155\pm0.0855</u>	0.9829 \pm 0.0056	0.0540 \pm 0.0232	<u>0.0336\pm0.0115</u>	0.9143 \pm 0.0281	0.348
DCFNet [56]	<u>3.0264\pm0.7397</u>	<u>2.1588\pm0.4563</u>	0.9051 \pm 0.0881	<u>0.9861\pm0.0038</u>	0.0781 \pm 0.0812	0.0508 \pm 0.0342	0.8771 \pm 0.1005	0.548
HFNet [44]	3.0826 \pm 0.6393	2.3112 \pm 0.5824	0.9121 \pm 0.8943	0.9842 \pm 0.0061	0.0253 \pm 0.0082	0.0431 \pm 0.0172	0.9343 \pm 0.0243	0.261
PanDiff [31]	3.2968 \pm 1.0016	2.4647 \pm 0.5837	0.8935 \pm 0.0863	0.9860 \pm 0.0063	0.0273 \pm 0.0123	0.0542 \pm 0.0264	0.9203 \pm 0.0360	261.410
PLRDiff [37]	4.3704 \pm 1.4709	3.4408 \pm 1.1747	0.8539 \pm 0.1330	0.9215 \pm 0.0362	0.1796 \pm 0.0369	0.1037 \pm 0.0269	0.7361 \pm 0.0505	40.142
KSDiff (ours)	2.8268\pm0.5153	2.0881\pm0.4538	0.9166\pm0.0831	0.9871\pm0.0034	0.0230 \pm 0.0090	0.0327\pm0.0154	0.9464\pm0.0234	0.079
Ideal value	0	0	1	1	0	0	1	0

4.1 Datasets, Metrics and Implementation Details

We validate our approach using datasets constructed following Wald’s protocol [8, 51], based on satellite data from WorldView-3 (WV3), GaoFen-2 (GF2), and QuickBird (QB). The data and preprocessing methods are obtained from the PanCollection repository [9]. We evaluate our method

Table 2: Result on the GF2 reduced-resolution dataset. The best results are highlighted in bold and the second best results are underlined.

Method	GaoFen-2			
	SAM (\pm std)	ERGAS (\pm std)	Q2 ⁿ (\pm std)	SCC (\pm std)
BDS-PC [47]	1.7110 \pm 0.3210	1.7025 \pm 0.4056	0.8932 \pm 0.0308	0.9448 \pm 0.0166
MTF-GLP-FS [49]	1.6757 \pm 0.3457	1.6023 \pm 0.3545	0.8914 \pm 0.0256	0.9390 \pm 0.0197
BT-H [11]	1.6810 \pm 0.3168	1.5524 \pm 0.3642	0.9089 \pm 0.0292	0.9508 \pm 0.0150
PNN [30]	1.0477 \pm 0.2264	1.0572 \pm 0.2355	0.9604 \pm 0.0100	0.9772 \pm 0.0054
DiCNN [14]	1.0525 \pm 0.1681	1.0812 \pm 0.2510	0.9594 \pm 0.0108	0.9781 \pm 0.0055
MSDCNN [54]	1.0472 \pm 0.2210	1.0413 \pm 0.2309	0.9612 \pm 0.0108	0.9782 \pm 0.0050
FusionNet [8]	0.9735 \pm 0.2117	0.9878 \pm 0.2222	0.9641 \pm 0.0093	0.9806 \pm 0.0049
CTINN [66]	0.8251 \pm 0.1386	0.9595 \pm 0.1068	0.9772 \pm 0.0117	0.9803 \pm 0.0015
LAGConv [17]	0.7859 \pm 0.1478	0.6869 \pm 0.1125	0.9804 \pm 0.0041	0.9843 \pm 0.0021
MMNet [67]	0.9292 \pm 0.1441	0.8117 \pm 0.1185	0.9690 \pm 0.0204	0.9859 \pm 0.0024
DCFNet [56]	0.8896 \pm 0.1577	0.8061 \pm 0.1369	0.9727 \pm 0.0100	0.9853 \pm 0.0024
HFNet [44]	0.8415 \pm 0.1517	0.7324 \pm 0.1301	0.9772 \pm 0.0114	0.9895 \pm 0.0020
PanDiff [31]	0.8881 \pm 0.1197	0.7461 \pm 0.1082	0.9727 \pm 0.0097	0.9887 \pm 0.0020
PLRDiff [37]	2.6755 \pm 2.0617	2.7434 \pm 2.4528	0.7938 \pm 0.1640	0.9055 \pm 0.0761
KSDiff (ours)	0.6980\pm0.1480	0.6782\pm0.1426	0.9831\pm0.0088	0.9899\pm0.0031
Ideal value	0	0	1	1

Table 3: Result on the QB reduced-resolution dataset. The best results are highlighted in bold and the second best results are underlined.

Method	QuickBird			
	SAM (\pm std)	ERGAS (\pm std)	Q2 ⁿ (\pm std)	SCC (\pm std)
BDS-PC [47]	8.2620 \pm 2.0497	7.5420 \pm 0.8138	0.8323 \pm 0.1013	0.9030 \pm 0.0181
MTF-GLP-FS [49]	8.1131 \pm 1.9553	7.5102 \pm 0.7926	0.8296 \pm 0.0905	0.8998 \pm 0.0196
BT-H [11]	7.1943 \pm 1.5523	7.4008 \pm 0.8378	0.8326 \pm 0.0880	0.9156 \pm 0.0152
PNN [30]	5.2054 \pm 0.9625	4.4722 \pm 0.3734	0.9180 \pm 0.0938	0.9711 \pm 0.0123
DiCNN [14]	5.3795 \pm 1.0266	5.1354 \pm 0.4876	0.9042 \pm 0.0942	0.9621 \pm 0.0133
MSDCNN [54]	5.1471 \pm 0.9342	4.3828 \pm 0.3400	0.9180 \pm 0.0966	0.9689 \pm 0.0121
FusionNet [8]	4.9226 \pm 0.9077	4.1594 \pm 0.3212	0.9252 \pm 0.0902	0.9755 \pm 0.0104
CTINN [66]	4.6583 \pm 0.7755	3.6969 \pm 0.2888	0.9320 \pm 0.0072	0.9829 \pm 0.0072
LAGConv [17]	4.5473 \pm 0.8296	3.8259 \pm 0.4196	0.9335 \pm 0.0878	0.9807 \pm 0.0091
MMNet [67]	4.5568 \pm 0.7285	3.6669 \pm 0.3036	0.9337 \pm 0.0941	0.9829 \pm 0.0070
DCFNet [56]	4.5383 \pm 0.7397	3.8315 \pm 0.2915	0.9325 \pm 0.0903	0.9741 \pm 0.0100
HFNet [44]	4.5396 \pm 0.8107	3.8123 \pm 0.3233	0.9339 \pm 0.0850	0.9804 \pm 0.0101
PanDiff [31]	4.5754 \pm 0.7359	3.7422 \pm 0.3099	0.9345\pm0.0902	0.9818 \pm 0.0902
PLRDiff [37]	26.8524 \pm 4.9881	47.4010 \pm 30.4469	0.2971 \pm 0.2461	0.6780 \pm 0.1504
KSDiff (ours)	4.5187\pm0.7711	3.6450\pm0.2865	0.9341\pm0.0837	0.9831\pm0.0072
Ideal value	0	0	1	1



Figure 5: Visualization of latent representations generated by KSDiff from PAN and LRMS images across different scenes.

using SAM [4], ERGAS [50], Q2ⁿ [12], and SCC [64] for reduced-resolution datasets, and HQNR [3], D_λ , and D_s for full-resolution datasets. The model is trained with the AdamW optimizer [28] on a single NVIDIA GeForce RTX 4090 GPU. Additional details on the datasets, evaluation metrics, compared methods, and training configurations are provided in the Suppl. Sec. C, including those related to the main experiments, ablation study, and discussion section.

4.2 Experimental Results

Our proposed KSDiff demonstrates superior performance through extensive evaluations on three benchmark datasets: WV3, GF2, and QB. Tables 1 to 3 compare KSDiff with state-of-the-art methods, including traditional, conventional DL-based, and diffusion-based approaches, confirming its robustness and ability to produce high-quality pan-sharpened images with fast inference. Visual comparisons in Fig. 4 show KSDiff’s results closely align with the ground truth. For more visualization results, please refer to the Suppl. Sec. F.

Table 4: Ablation study on the WV3 reduced-resolution dataset. The best results are highlighted.

Method	Ablation				Metrics				Runtime (s)
	Diffusion Prior	PLFE	Tensor Structure	Joint-Training	SAM (\pm std)	ERGAS (\pm std)	Q2 ⁿ (\pm std)	SCC (\pm std)	
PanNeXt-U	✗	✗	✗	✗	2.9515 \pm 0.5898	2.2204 \pm 0.5563	0.9135 \pm 0.0815	0.9841 \pm 0.0046	0.036
Entangled Feature	✓	✓	✓	✓	2.9419 \pm 0.5356	2.1767 \pm 0.4643	0.9139 \pm 0.0834	0.9844 \pm 0.0054	0.080
w/o Structure-Aware	✓	✓	✗	✓		Cannot			
Separate-Training	✓	✓	✓	✗	2.9149 \pm 0.5233	2.1677 \pm 0.4678	0.9141 \pm 0.0835	0.9851 \pm 0.0047	0.079
KSDiff (ours)	✓	✓	✓	✓	2.8268\pm0.5153	2.0881\pm0.4538	0.9166\pm0.0831	0.9871\pm0.0034	0.079
Ideal value	-	-	-	-	0	0	1	1	0

4.3 Ablation Study

To validate the effectiveness of each component in our proposed method, we conducted ablation studies, with results summarized in Table 4.

Firstly, to assess the impact of the latent diffusion prior, we evaluated the original PanNeXt-U network without incorporating the latent representation generated by the diffusion model. The results demonstrate that omitting the latent representation compromises performance, despite a reduction in latency. Secondly, we ablated the proposed Pyramid Latent Fusion Encoder (PLFE) by replacing it with an encoder that directly concatenates the PAN, LRMS, and GT images as input. This substitution led to degraded performance, highlighting the importance of PLFE in our framework. We further

investigated the tensor structure-aware kernel generator by replacing it with a multi-layer perceptron (MLP) containing an equivalent number of intermediate features. This modification increased the number of learnable parameters by over tenfold, resulting in convergence failure, underscoring the efficiency and necessity of our tensor-aware design. Finally, to evaluate the joint training strategy in the diffusion model training stage, we conducted an ablation by first training the diffusion model to learn the latent representation independently and then integrating it with a pre-trained regression network for testing. This approach yielded inferior performance compared to our joint training strategy, confirming its critical role in achieving optimal results.

Table 5: Result of replacing convolution modules in other backbones with KSDiff on WV3 reduced-resolution dataset.

Method	Metrics			
	SAM (\pm std)	ERGAS (\pm std)	Q ² (\pm std)	SCC (\pm std)
DiCNN [14]	3.5929 \pm 0.7623	2.6733 \pm 0.6627	0.9004 \pm 0.0871	0.9763 \pm 0.0072
DiCNN+KSDiff	3.4534 \pm 0.6957	2.5623 \pm 0.6328	0.9037 \pm 0.0865	0.9785 \pm 0.0070
FusionNet [8]	3.3252 \pm 0.6978	2.4666 \pm 0.6446	0.9044 \pm 0.0904	0.9807 \pm 0.0069
FusionNet+KSDiff	3.1475 \pm 0.5630	2.3106 \pm 0.5381	0.9055 \pm 0.0866	0.9829 \pm 0.0052
LAGNet [17]	3.1042 \pm 0.5585	2.2999 \pm 0.6120	0.9098 \pm 0.0842	0.9830 \pm 0.0068
LAGNet+KSDiff	3.0023 \pm 0.5723	2.2314 \pm 0.5762	0.9122 \pm 0.0862	0.9835 \pm 0.0067
Ideal value	0	0	1	1

Table 6: Impact of low-rank core tensor size (r_1, r_2, r_3, r_4) on the WV3 reduced-resolution dataset.

Size	Metrics			
	SAM (\pm std)	ERGAS (\pm std)	Q ² (\pm std)	SCC (\pm std)
(4, 4, 1, 1)	3.0921 \pm 0.5376	2.2896 \pm 0.5005	0.9104 \pm 0.0843	0.9833 \pm 0.0053
(4, 4, 2, 2)	3.0622 \pm 0.5362	2.2725 \pm 0.4996	0.9111 \pm 0.0839	0.9837 \pm 0.0051
(8, 8, 1, 1)	3.1275 \pm 0.5616	2.3009 \pm 0.5251	0.9057 \pm 0.0894	0.9828 \pm 0.0050
(8, 8, 2, 2)	3.1040 \pm 0.5433	2.2988 \pm 0.5158	0.9096 \pm 0.0854	0.9833 \pm 0.0056
(16, 16, 1, 1)	3.1520 \pm 0.5644	2.3146 \pm 0.5277	0.9052 \pm 0.0873	0.9827 \pm 0.0066
(16, 16, 2, 2)	3.1475 \pm 0.5630	2.3106 \pm 0.5381	0.9055 \pm 0.0866	0.9829 \pm 0.0052
Ideal value	0	0	1	1

4.4 Discussions

Latent Representation Visualization. As shown in Fig. 5, we visualize latent diffusion representations from PAN and LRMS image pairs across diverse scenes. Representations from ocean-dominated images (left two subfigures) exhibit similar distributions, as do those from building and land-dominated images (right two subfigures), with variations due to building density. This demonstrates the diffusion model’s ability to effectively capture intrinsic global information in PAN and LRMS images.

Replacing Standard Convolution. To assess the effectiveness of KSDiff in enhancing pansharpening networks, we substituted convolutional layers in various pansharpening backbones with KSDiff. The results, shown in Table 5, indicate that KSDiff consistently improves the performance of DiCNN [14], FusionNet [8], and LAGNet [17].

Size of Low-Rank Core Tensor. To investigate the impact of the low-rank core tensor $\mathcal{G} \in \mathbb{R}^{r_1 \times r_2 \times r_3 \times r_4}$ size on performance, we conducted experiments on the WV3 reduced-resolution dataset by varying its scale. For experiment efficiency, we selected FusionNet [8] as the base model and replaced its backbone with our KSDiff-enhanced backbone. The results for different core tensor sizes are presented in Table 6. Notably, a smaller core tensor is already effective and can even outperform larger core tensors when trained under the same experimental conditions. This behavior resembles that of LoRA [16], which efficiently fine-tunes linear layers in large language models using low-rank matrices. However, as shown in Table 6, when the sizes of the first two modes (input and output channels) are fixed and the last two modes (kernel size) are increased from 1 to 2, performance improves. A plausible explanation can be that a tensor of size $(r_1, r_2, 1, 1)$ reduces to a 2D matrix, losing the structural benefits of a 4D tensor. This suggests that preserving the structural integrity of higher-dimensional tensors in parameter space could be helpful for enhancing model performance.

5 Conclusion

In conclusion, we proposed KSDiff, a novel kernel space diffusion model that enhances pansharpening by generating globally aware convolutional kernels through a diffusion process in latent space. By integrating a convolution core generator, a unified factor generator, and a structure-aware multi-head attention mechanism, KSDiff effectively balances high-quality fusion with fast inference. Extensive experiments on WorldView-3, GaoFen-2, and QuickBird datasets demonstrate its superior performance in both spatial and spectral fidelity, offering a practical and scalable solution for remote sensing image fusion.

References

- [1] Bruno Aiazzi, Luciano Alparone, Stefano Baronti, Andrea Garzelli, and Massimo Selva. Mtf-tailored multiscale fusion of high-resolution ms and pan imagery. *Photogrammetric Engineering & Remote Sensing*, 72(5):591–596, 2006.
- [2] Michael S Albergo, Nicholas M Boffi, and Eric Vanden-Eijnden. Stochastic interpolants: A unifying framework for flows and diffusions. *arXiv preprint arXiv:2303.08797*, 2023.
- [3] Alberto Arienzo, Gemine Vivone, Andrea Garzelli, Luciano Alparone, and Jocelyn Chanussot. Full-resolution quality assessment of pansharpening: Theoretical and hands-on approaches. *IEEE Geoscience and Remote Sensing Magazine*, 10(3):168–201, 2022.
- [4] Joseph W Boardman. Automating spectral unmixing of aviris data using convex geometry concepts. In *JPL, Summaries of the 4th Annual JPL Airborne Geoscience Workshop. Volume 1: AVIRIS Workshop*, 1993.
- [5] Zihan Cao, Shiqi Cao, Liang-Jian Deng, Xiao Wu, Junming Hou, and Gemine Vivone. Diffusion model with disentangled modulations for sharpening multispectral and hyperspectral images. *Information Fusion*, 104:102158, 2024.
- [6] Hyungjin Chung, Jeongsol Kim, Michael T Mccann, Marc L Klasky, and Jong Chul Ye. Diffusion posterior sampling for general noisy inverse problems. *arXiv preprint arXiv:2209.14687*, 2022.
- [7] Valentin De Bortoli, James Thornton, Jeremy Heng, and Arnaud Doucet. Diffusion schrödinger bridge with applications to score-based generative modeling. *Advances in Neural Information Processing Systems*, 34:17695–17709, 2021.
- [8] Liang-Jian Deng, Gemine Vivone, Cheng Jin, and Jocelyn Chanussot. Detail injection-based deep convolutional neural networks for pansharpening. *IEEE Transactions on Geoscience and Remote Sensing*, 59(8):6995–7010, 2020.
- [9] Liang-Jian Deng, Gemine Vivone, Mercedes E Paoletti, Giuseppe Scarpa, Jiang He, Yongjun Zhang, Jocelyn Chanussot, and Antonio Plaza. Machine learning in pansharpening: A benchmark, from shallow to deep networks. *IEEE Geoscience and Remote Sensing Magazine*, 10(3): 279–315, 2022.
- [10] Yule Duan, Xiao Wu, Haoyu Deng, and Liang-Jian Deng. Content-adaptive non-local convolution for remote sensing pansharpening. In *Proceedings of the IEEE/CVF Conference on Computer Vision and Pattern Recognition*, pages 27738–27747, 2024.
- [11] Patrick Esser, Sumith Kulal, Andreas Blattmann, Rahim Entezari, Jonas Müller, Harry Saini, Yam Levi, Dominik Lorenz, Axel Sauer, Frederic Boesel, et al. Scaling rectified flow transformers for high-resolution image synthesis. In *Forty-first international conference on machine learning*, 2024.
- [12] Andrea Garzelli and Filippo Nencini. Hypercomplex quality assessment of multi/hyperspectral images. *IEEE Geoscience and Remote Sensing Letters*, 6(4):662–665, 2009.
- [13] Chunming He, Kai Li, Guoxia Xu, Jiangpeng Yan, Longxiang Tang, Yulun Zhang, Yaowei Wang, and Xiu Li. Hqg-net: Unpaired medical image enhancement with high-quality guidance. *IEEE Transactions on Neural Networks and Learning Systems*, 2023.
- [14] Lin He, Yizhou Rao, Jun Li, Jocelyn Chanussot, Antonio Plaza, Jiawei Zhu, and Bo Li. Pansharpening via detail injection based convolutional neural networks. *IEEE Journal of Selected Topics in Applied Earth Observations and Remote Sensing*, 12(4):1188–1204, 2019.
- [15] Jonathan Ho, Ajay Jain, and Pieter Abbeel. Denoising diffusion probabilistic models. *Advances in neural information processing systems*, 33:6840–6851, 2020.
- [16] Edward J Hu, Yelong Shen, Phillip Wallis, Zeyuan Allen-Zhu, Yuanzhi Li, Shean Wang, Lu Wang, and Weizhu Chen. LoRA: Low-rank adaptation of large language models. In *International Conference on Learning Representations*, 2022. URL <https://openreview.net/forum?id=nZeVKeeFYf9>.

- [17] Zi-Rong Jin, Tian-Jing Zhang, Tai-Xiang Jiang, Gemine Vivone, and Liang-Jian Deng. Lagconv: Local-context adaptive convolution kernels with global harmonic bias for pansharpening. In *Proceedings of the AAAI conference on artificial intelligence*, volume 36, pages 1113–1121, 2022.
- [18] Tero Karras, Miika Aittala, Timo Aila, and Samuli Laine. Elucidating the design space of diffusion-based generative models. *Advances in neural information processing systems*, 35: 26565–26577, 2022.
- [19] Angelos Katharopoulos, Apoorv Vyas, Nikolaos Pappas, and François Fleuret. Transformers are rnns: Fast autoregressive transformers with linear attention. In *International conference on machine learning*, pages 5156–5165. PMLR, 2020.
- [20] Diederik P Kingma, Max Welling, et al. Auto-encoding variational bayes, 2013.
- [21] Tamara G Kolda and Brett W Bader. Tensor decompositions and applications. *SIAM review*, 51(3):455–500, 2009.
- [22] P Kwarteng and A Chavez. Extracting spectral contrast in landsat thematic mapper image data using selective principal component analysis. *Photogramm. Eng. Remote Sens*, 55(1):339–348, 1989.
- [23] Yixun Liang, Ping Zhang, Yang Mei, and Tingqi Wang. Pmacnet: Parallel multiscale attention constraint network for pan-sharpening. *IEEE Geoscience and Remote Sensing Letters*, 19:1–5, 2022.
- [24] Yaron Lipman, Ricky TQ Chen, Heli Ben-Hamu, Maximilian Nickel, and Matt Le. Flow matching for generative modeling. *arXiv preprint arXiv:2210.02747*, 2022.
- [25] Jiawei Liu, Qiang Wang, Huijie Fan, Yinong Wang, Yandong Tang, and Liangqiong Qu. Residual denoising diffusion models. In *Proceedings of the IEEE/CVF Conference on Computer Vision and Pattern Recognition*, pages 2773–2783, 2024.
- [26] Xingchao Liu, Chengyue Gong, and Qiang Liu. Flow straight and fast: Learning to generate and transfer data with rectified flow. *arXiv preprint arXiv:2209.03003*, 2022.
- [27] Zhuang Liu, Hanzi Mao, Chao-Yuan Wu, Christoph Feichtenhofer, Trevor Darrell, and Saining Xie. A convnet for the 2020s. In *Proceedings of the IEEE/CVF conference on computer vision and pattern recognition*, pages 11976–11986, 2022.
- [28] Ilya Loshchilov and Frank Hutter. Decoupled weight decay regularization. *arXiv preprint arXiv:1711.05101*, 2017.
- [29] Cheng Lu, Yuhao Zhou, Fan Bao, Jianfei Chen, Chongxuan Li, and Jun Zhu. Dpm-solver: A fast ode solver for diffusion probabilistic model sampling in around 10 steps. *Advances in Neural Information Processing Systems*, 35:5775–5787, 2022.
- [30] Giuseppe Masi, Davide Cozzolino, Luisa Verdoliva, and Giuseppe Scarpa. Pansharpening by convolutional neural networks. *Remote Sensing*, 8(7):594, 2016.
- [31] Qingyan Meng, Wenxu Shi, Sijia Li, and Linlin Zhang. Pandiff: A novel pansharpening method based on denoising diffusion probabilistic model. *IEEE Transactions on Geoscience and Remote Sensing*, 61:1–17, 2023.
- [32] Xiangchao Meng, Jie Li, Huanfeng Shen, Liangpei Zhang, and Hongyan Zhang. Pansharpening with a guided filter based on three-layer decomposition. *Sensors*, 16(7):1068, 2016.
- [33] Xavier Otazu, María González-Audícana, Octavi Fors, and Jorge Núñez. Introduction of sensor spectral response into image fusion methods. application to wavelet-based methods. *IEEE Transactions on Geoscience and Remote Sensing*, 43(10):2376–2385, 2005.
- [34] Siran Peng, Liang-Jian Deng, Jin-Fan Hu, and Yu-Wei Zhuo. Source-adaptive discriminative kernels based network for remote sensing pansharpening. In *IJCAI*, pages 1283–1289, 2022.

- [35] Robin Rombach, Andreas Blattmann, Dominik Lorenz, Patrick Esser, and Björn Ommer. High-resolution image synthesis with latent diffusion models. In *Proceedings of the IEEE/CVF conference on computer vision and pattern recognition*, pages 10684–10695, 2022.
- [36] Olaf Ronneberger, Philipp Fischer, and Thomas Brox. U-net: Convolutional networks for biomedical image segmentation. In *Medical image computing and computer-assisted intervention–MICCAI 2015: 18th international conference, Munich, Germany, October 5-9, 2015, proceedings, part III* 18, pages 234–241. Springer, 2015.
- [37] Xiangyu Rui, Xiangyong Cao, Li Pang, Zeyu Zhu, Zongsheng Yue, and Deyu Meng. Unsupervised hyperspectral pansharpening via low-rank diffusion model. *Information Fusion*, 107: 102325, 2024.
- [38] Chitwan Saharia, Jonathan Ho, William Chan, Tim Salimans, David J Fleet, and Mohammad Norouzi. Image super-resolution via iterative refinement. *IEEE transactions on pattern analysis and machine intelligence*, 45(4):4713–4726, 2022.
- [39] Neta Shaul, Juan Perez, Ricky TQ Chen, Ali Thabet, Albert Pumarola, and Yaron Lipman. Bespoke solvers for generative flow models. *arXiv preprint arXiv:2310.19075*, 2023.
- [40] Zhuoran Shen, Mingyuan Zhang, Haiyu Zhao, Shuai Yi, and Hongsheng Li. Efficient attention: Attention with linear complexities. In *Proceedings of the IEEE/CVF winter conference on applications of computer vision*, pages 3531–3539, 2021.
- [41] Jiaming Song, Chenlin Meng, and Stefano Ermon. Denoising diffusion implicit models. *arXiv preprint arXiv:2010.02502*, 2020.
- [42] Yang Song, Jascha Sohl-Dickstein, Diederik P Kingma, Abhishek Kumar, Stefano Ermon, and Ben Poole. Score-based generative modeling through stochastic differential equations. *arXiv preprint arXiv:2011.13456*, 2020.
- [43] Yang Song, Prafulla Dhariwal, Mark Chen, and Ilya Sutskever. Consistency models. 2023.
- [44] Jiangtong Tan, Jie Huang, Naishan Zheng, Man Zhou, Keyu Yan, Danfeng Hong, and Feng Zhao. Revisiting spatial-frequency information integration from a hierarchical perspective for panchromatic and multi-spectral image fusion. In *Proceedings of the IEEE/CVF Conference on Computer Vision and Pattern Recognition*, pages 25922–25931, 2024.
- [45] Ledyard R Tucker. Some mathematical notes on three-mode factor analysis. *Psychometrika*, 31(3):279–311, 1966.
- [46] Ashish Vaswani, Noam Shazeer, Niki Parmar, Jakob Uszkoreit, Llion Jones, Aidan N Gomez, Łukasz Kaiser, and Illia Polosukhin. Attention is all you need. *Advances in neural information processing systems*, 30, 2017.
- [47] Gemine Vivone. Robust band-dependent spatial-detail approaches for panchromatic sharpening. *IEEE transactions on Geoscience and Remote Sensing*, 57(9):6421–6433, 2019.
- [48] Gemine Vivone, Rocco Restaino, and Jocelyn Chanussot. A regression-based high-pass modulation pansharpening approach. *IEEE Transactions on geoscience and remote sensing*, 56(2): 984–996, 2017.
- [49] Gemine Vivone, Rocco Restaino, and Jocelyn Chanussot. Full scale regression-based injection coefficients for panchromatic sharpening. *IEEE Transactions on Image Processing*, 27(7): 3418–3431, 2018.
- [50] Lucien Wald. *Data fusion: definitions and architectures: fusion of images of different spatial resolutions*. Presses des MINES, 2002.
- [51] Lucien Wald, Thierry Ranchin, and Marc Mangolini. Fusion of satellite images of different spatial resolutions: Assessing the quality of resulting images. *Photogrammetric engineering and remote sensing*, 63(6):691–699, 1997.

- [52] Jianyi Wang, Zongsheng Yue, Shangchen Zhou, Kelvin CK Chan, and Chen Change Loy. Exploiting diffusion prior for real-world image super-resolution. *International Journal of Computer Vision*, 132(12):5929–5949, 2024.
- [53] Kai Wang, Dongwen Tang, Boya Zeng, Yida Yin, Zhaopan Xu, Yukun Zhou, Zelin Zang, Trevor Darrell, Zhuang Liu, and Yang You. Neural network diffusion. *arXiv preprint arXiv:2402.13144*, 2024.
- [54] Yancong Wei, Qiangqiang Yuan, Xiangchao Meng, Huanfeng Shen, Liangpei Zhang, and Michael Ng. Multi-scale-and-depth convolutional neural network for remote sensed imagery pan-sharpening. In *2017 IEEE International Geoscience and Remote Sensing Symposium (IGARSS)*, pages 3413–3416. IEEE, 2017.
- [55] Chen Wu, Bo Du, Xiaohui Cui, and Liangpei Zhang. A post-classification change detection method based on iterative slow feature analysis and bayesian soft fusion. *Remote Sensing of Environment*, 199:241–255, 2017.
- [56] Xiao Wu, Ting-Zhu Huang, Liang-Jian Deng, and Tian-Jing Zhang. Dynamic cross feature fusion for remote sensing pansharpening. In *Proceedings of the IEEE/CVF International Conference on Computer Vision*, pages 14687–14696, 2021.
- [57] Zhong-Cheng Wu, Ting-Zhu Huang, Liang-Jian Deng, Jie Huang, Jocelyn Chanussot, and Gemine Vivone. Lrtcfpan: Low-rank tensor completion based framework for pansharpening. *IEEE Transactions on Image Processing*, 32:1640–1655, 2023.
- [58] Zhong-Cheng Wu, Ting-Zhu Huang, Liang-Jian Deng, and Gemine Vivone. A framelet sparse reconstruction method for pansharpening with guaranteed convergence. *Inverse Problems and Imaging*, 17(6):1277–1300, 2023.
- [59] Bin Xia, Yulun Zhang, Shiyin Wang, Yitong Wang, Xinglong Wu, Yapeng Tian, Wenming Yang, and Luc Van Gool. Diffir: Efficient diffusion model for image restoration. In *Proceedings of the IEEE/CVF International Conference on Computer Vision*, pages 13095–13105, 2023.
- [60] Junfeng Yang, Xueyang Fu, Yuwen Hu, Yue Huang, Xinghao Ding, and John Paisley. Pannet: A deep network architecture for pan-sharpening. In *Proceedings of the IEEE international conference on computer vision*, pages 5449–5457, 2017.
- [61] Xiaohui Yuan, Jianfang Shi, and Lichuan Gu. A review of deep learning methods for semantic segmentation of remote sensing imagery. *Expert Systems with Applications*, 169:114417, 2021.
- [62] Zongsheng Yue, Jianyi Wang, and Chen Change Loy. Resshift: Efficient diffusion model for image super-resolution by residual shifting. *Advances in Neural Information Processing Systems*, 36:13294–13307, 2023.
- [63] Kaiwen Zheng, Cheng Lu, Jianfei Chen, and Jun Zhu. Dpm-solver-v3: Improved diffusion ode solver with empirical model statistics. *Advances in Neural Information Processing Systems*, 36: 55502–55542, 2023.
- [64] Jie Zhou, Daniel L Civco, and John A Silander. A wavelet transform method to merge landsat tm and spot panchromatic data. *International journal of remote sensing*, 19(4):743–757, 1998.
- [65] Linqi Zhou, Aaron Lou, Samar Khanna, and Stefano Ermon. Denoising diffusion bridge models. *arXiv preprint arXiv:2309.16948*, 2023.
- [66] Man Zhou, Jie Huang, Yanchi Fang, Xueyang Fu, and Aiping Liu. Pan-sharpening with customized transformer and invertible neural network. In *Proceedings of the AAAI conference on artificial intelligence*, volume 36, pages 3553–3561, 2022.
- [67] Man Zhou, Keyu Yan, Jinshan Pan, Wenqi Ren, Qi Xie, and Xiangyong Cao. Memory-augmented deep unfolding network for guided image super-resolution. *International Journal of Computer Vision*, 131(1):215–242, 2023.